The Astrophysical Journal, 902:6 (15pp), 2020 October 10 https://doi.org/10.3847/1538-4357/abb247

SN 2018fif: The Explosion of a Large Red Supergiant Discovered in Its Infancy by the Zwicky Transient Facility

Maayane T. Soumagnac[1,2], Noam Ganot[1], Ido Irani[1], Avishay Gal-yam[1], Eran O. Ofek[1], Eli Waxman[1], Jonathan Morag[1], Ofer Yaron[1], Steve Schulze[1], Yi Yang[1], Adam Rubin[3], S. Bradley Cenko[4,5], Jesper Sollerman[6], Daniel A. Perley[7], Christoffer Fremling[8], Peter Nugent[2,9], James D. Neill[10], Emir Karamehmetoglu[6], Eric C. Bellm[11], Rachel J. Bruch[1], Rick Burruss[12], Virginia Cunningham[13], Richard Dekany[14], V. Zach Golkhou[11,15,20], Matthew J. Graham[8], Mansi M. Kasliwal[8], Nicholas P Konidaris[10], Shrinivas R. Kulkarni[8], Thomas Kupfer[16], Russ R. Laher[17], Frank J. Masci[17], Reed Riddle[14], Mickael Rigault[18], Ben Rusholme[17], Jan van Roestel[8], and Barak Zackay[19]

[1] Department of Particle Physics and Astrophysics, Weizmann Institute of Science, Rehovot 76100, Israel; mtsoumagnac@lbl.gov
[2] Lawrence Berkeley National Laboratory, 1 Cyclotron Road, Berkeley, CA 94720, USA
[3] European Southern Observatory, Karl-Schwarzschild-Str 2, D-85748 Garching bei Munchen, Germany
[4] Astrophysics Science Division, NASA Goddard Space Flight Center, MC 661, Greenbelt, MD 20771, USA
[5] Joint Space-Science Institute, University of Maryland, College Park, MD 20742, USA
[6] The Oskar Klein Centre, Department of Astronomy, Stockholm University, AlbaNova, SE-10691 Stockholm, Sweden
[7] Astrophysics Research Institute, Liverpool John Moores University, 146 Brownlow Hill, Liverpool L3 5RF, UK
[8] Division of Physics, Mathematics and Astronomy, California Institute of Technology, Pasadena, CA 91125, USA
[9] Department of Astronomy, University of California, Berkeley, CA 94720-3411, USA
[10] Observatories of the Carnegie Institution for Science, 813 Santa Barbara Street, Pasadena, CA 91101, USA
[11] DIRAC Institute, Department of Astronomy, University of Washington, 3910 15th Avenue NE, Seattle, WA 98195, USA
[12] Caltech Optical Observatories, Palomar Mountain, CA 92060, USA
[13] Astronomy Department, University of Maryland, College Park, MD 20742, USA
[14] Caltech Optical Observatories, California Institute of Technology, Pasadena, CA 91125, USA
[15] The eScience Institute, University of Washington, Seattle, WA 98195, USA
[16] Kavli Institute for Theoretical Physics, University of California, Santa Barbara, CA 93106, USA
[17] IPAC, California Institute of Technology, 1200 E. California Blvd, Pasadena, CA 91125, USA
[18] Université Clermont Auvergne, CNRS/IN2P3, Laboratoire de Physique de Clermont, F-63000 Clermont-Ferrand, France
[19] Institute for Advanced Study, 1 Einstein Drive, Princeton, NJ 08540, USA
Received 2019 July 24; revised 2020 August 17; accepted 2020 August 23; published 2020 October 7

Abstract

High-cadence transient surveys are able to capture supernovae closer to their first light than ever before. Applying analytical models to such early emission, we can constrain the progenitor stars' properties. In this paper, we present observations of SN 2018fif (ZTF 18abokyfk). The supernova was discovered close to first light and monitored by the Zwicky Transient Facility (ZTF) and the Neil Gehrels Swift Observatory. Early spectroscopic observations suggest that the progenitor of SN 2018fif was surrounded by relatively small amounts of circumstellar material compared to all previous cases. This particularity, coupled with the high-cadence multiple-band coverage, makes it a good candidate to investigate using shock-cooling models. We employ the SOPRANOS code, an implementation of the model by Sapir & Waxman and its extension to early times by Morag et al. Compared with previous implementations, SOPRANOS has the advantage of including a careful account of the limited temporal validity domain of the shock-cooling model as well as allowing usage of the entirety of the early UV data. We find that the progenitor of SN 2018fif was a large red supergiant with a radius of $R = 744.0^{+183.0}_{-128.0}\,R_{\odot}$ and an ejected mass of $M_{\rm ej} = 9.3^{+0.4}_{-5.8}\,M_{\odot}$. Our model also gives information on the explosion epoch, the progenitor's inner structure, the shock velocity, and the extinction. The distribution of radii is double-peaked, with smaller radii corresponding to lower values of the extinction, earlier recombination times, and a better match to the early UV data. If these correlations persist in future objects, denser spectroscopic monitoring constraining the time of recombination, as well as accurate UV observations (e.g., with ULTRASAT), will help break the extinction/radius degeneracy and independently determine both.

Unified Astronomy Thesaurus concepts: Supernovae (1668); Type II supernovae (1731); Astronomy data modeling (1859); Observational astronomy (1145); Ultraviolet transient sources (1854); Transient sources (1851)

Supporting material: machine-readable table

1. Introduction

In recent years, advances in the field of high-cadence transient surveys have made it possible to systematically discover and follow up supernovae (SNe) within hours of their first light (e.g., Nugent et al. 2011; Gal-Yam et al. 2014; Arcavi et al. 2017; Tartaglia et al. 2017; Yaron et al. 2017). This offers new opportunities to understand the early stages of core-collapse (CC) SN explosions and to identify the nature of their progenitor stars.

First, rapid spectroscopic follow-up in the hours following first light has led to the detection of "flash ionized" emission from infant SNe (Gal-Yam et al. 2014; Shivvers et al. 2015; Khazov et al. 2016; Yaron et al. 2017; Hosseinzadeh et al. 2018). These events show prominent, transient, high-ionization recombination emission lines in their spectra, a signature of circumstellar material (CSM) ionized by the SN shock-breakout flash ("flash spectroscopy").

[20] Moore-Sloan, WRF Innovation in Data Science, and DIRAC Fellow.

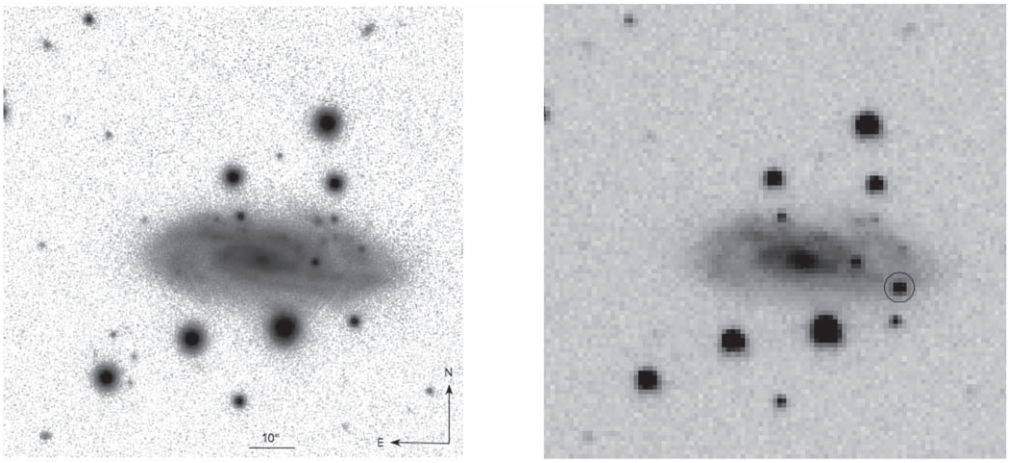

Figure 1. Left: the PS1 *r*-band image[22] of UGC 85, the host galaxy of the supernova SN 2018fif. Right: the P48 *r*-band image of SN 2018fif on 2018 September 4 at 9:26:50.00 UT. The circle is centered on the SN position.

Khazov et al. (2016) showed that ∼20% of the SNe discovered by the Palomar Transient Factory (PTF) within 10 days of explosion are "flashers," while recent results from the Zwicky Transient Facility (ZTF; R. J. Bruch et al. 2020, in preparation) suggest that the fraction of such events may be even higher for events observed earlier, and that CSM around CC SNe progenitors is common.

Second, observational access to the first hours following the explosion has offered a new opportunity to test theoretical models of early emission from CC SNe and constrain their progenitor properties. The handful of cases where direct pre-explosion observations of progenitors exist (e.g., Smartt 2015, and references therein) suggest that many Type II SNe arise from red supergiants, a population of stars with radii ranging from about $100\,R_\odot$ to $1500\,R_\odot$ (e.g., Levesque 2017, and references therein). In recent years, theorists have developed analytical models linking early multicolor light curves of SNe to progenitor properties, such as radius, mass, or inner structure. Papers by Morozova et al. (2016) and Rubin & Gal-Yam (2017) review and compare these models. In this paper, we use the analytical model by Sapir & Waxman (2017, hereafter SW17) and its extension by J. Morag et al. (2020, in preparation, hereafter M20), which has two advantages. First, it accounts for bound–free absorption in the calculation of the color temperature, a feature that may have a large impact on the estimation of the progenitor radius. Second, it extends the previous results by Rabinak & Waxman (2011) to later times, making additional observations useful in this analysis. M20 further extends the results of SW17 to the times immediately following breakout, allowing one to use all the available early data.

Comparisons between early observations of CC SNe and theoretical predictions from analytical models were reported previously (e.g., by Gall et al. 2015; González-Gaitán et al. 2015; Rubin & Gal-Yam 2017; Hosseinzadeh et al. 2019) but these authors fit only a fixed range of times in the early light curve. Rubin & Gal-Yam (2017) optimize the number of observations included in the fit based on the limited temporal validity domain of these analytical models, but their observations were limited to the *r* band. Recently, Ricks & Dwarkadas (2019), Martinez & Bersten (2019), Goldberg et al. (2019), Dessart & Hillier (2019), and Eldridge et al. (2019) have compared observations to hydrodynamic models on simulated progenitors exploded "by hand."

To our knowledge, SN 2013fs (Yaron et al. 2017) is the only published object for which high-cadence multiple-band observations are available and which was modeled with an analytical model using the methodology of Rubin & Gal-Yam (2017; see Section 4.3 for a detailed discussion on this aspect of the modeling). However, the spectroscopic observations of SN 2013 fs —the best observed "flasher" to date—show evidence for $\sim 10^{-3}\,M_\odot$ of confined CSM surrounding the progenitor. The presence of CSM casts doubt upon the validity of the SW17 model in this case, and perhaps could have pushed the best-fit model radius found for this object ($R = 100$–$350\ R_\odot$) toward the lower end of the radius distribution of red supergiants. A "cleaner" supernova, with no prominent signatures of CSM around the progenitor, may be a more appropriate test case for the SW17 model.

In this paper, we present and analyze the UV and visible-light observations of SN 2018fif (ZTF 18abokyfk), an SN first detected shortly after explosion by the ZTF (e.g., Bellm et al. 2019; Graham et al. 2019) as part of the ZTF extragalactic high-cadence experiment (Gal-Yam 2019).

We present the aforementioned observations of SN 2018fif in Section 2. In Section 3, we present our analysis of these observations, and the spectroscopic evidence making SN 2018fif a good candidate for modeling. Section 4 is dedicated to the modeling of the shock-cooling phase of SN 2018fif and the derivation of the progenitor parameters. We then summarize our main results in Section 5.

2. Observations and Data Reduction

In this section, we present the observations of SN 2018fif by ZTF and the Neil Gehrels Swift Observatory (Swift).

2.1. Discovery

SN 2018fif was first detected on 2018 August 21 at 8:46 UT by the ZTF wide-field camera mounted on the 1.2 m Samuel Oschin Telescope (P48) at Palomar Observatory. ZTF images were processed and calibrated by the ZTF pipeline (Masci et al. 2019). A duty astronomer reviewing the ZTF alert stream (Patterson et al. 2019) via the ZTF GROWTH Marshal (Kasliwal et al. 2019) issued an internal alert, triggering follow-up with multiple telescopes, using the methodology of Gal-Yam et al. (2011). This event was reported by Fremling (2018) and designated SN 2018fif by the IAU Transient Server (TNS[21]). The SN is associated with the $B = 14.5$ mag galaxy UGC 85 (Falco et al. 1999), shown in

[21] https://wis-tns.weizmann.ac.il/
[22] http://ps1images.stsci.edu

Table 1
Basic Parameters of SN 2018fif

Parameter	Value
R.A. α (J2000)	2.°360644
Decl. δ (J2000)	47.°354093
Redshift z	0.017189
Distance modulus μ	34.31 mag
Galactic extinction E_{B-V}	0.10 mag

Figure 1. The coordinates of the object measured in the ZTF images are $\alpha = 00^{\rm h}09^{\rm m}26\overset{\rm s}{.}55$, $\delta = +47^{\rm d}21'14\overset{''}{.}7$ (J2000.0). The redshift $z = 0.017189$ and the distance modulus $\mu = 34.31$ mag were obtained from the NASA/IPAC Extragalactic Database (NED) and the extinction was deduced from Schlafly & Finkbeiner (2011) and using the extinction curves of Cardelli et al. (1989). These parameters are summarized in Table 1.

Previous ZTF observations were obtained in the months prior to the SN explosion and the most recent nondetection was on 2018 August 20 at 9:37:26.40 UT, i.e., less than 24 hr before the first detection. We present a derivation of the explosion epoch in Section 3.1.

2.2. Photometry

SN 2018fif was photometrically followed in multiple bands for ∼5 months. Light curves are shown in Figure 2. The photometry is reported in Table 2 and is electronically available from the Weizmann Interactive Supernova Data Repository[23] (WISeREP, Yaron & Gal-Yam 2012).

Swift (Gehrels et al. 2004) observations of the SN 2018fif field started on 2018 August 21 and 11 observations were obtained with a cadence of ∼1 day.

Observations from P48 were obtained using the ZTF mosaic camera composed of 16 6K × 6K CCDs (e.g., Bellm et al. 2015) through r-band and g-band filters of the Sloan Digital Sky Survey (SDSS). Data were obtained with a cadence of three to six observations per day, to a limiting magnitude of $R \approx 20.5$ mag[AB]. ZTF data were reduced using the ZTF photometric pipeline (Masci et al. 2019) employing the optimal image subtraction algorithm of Zackay et al. (2016).

Observations from the robotic 1.52 m telescope at Palomar (P60; Cenko et al. 2006) were obtained using the rainbow camera arm of the SED Machine spectrograph (Blagorodnova et al. 2018), equipped with a 2048 × 2048 pixel CCD camera and g', r', and i' SDSS filters. P60 data were reduced using the FPipe pipeline (Fremling et al. 2016).

The UVOT data were retrieved from the NASA Swift Data Archive[24] and reduced using standard software distributed with HEAsoft version 6.26.[25] Photometry was measured using the FTOOLSs uvotimsum and uvotsource with a 3″ circular aperture. To remove the host contribution, we obtained and coadded two final epoch in all broadband filters and built a host template using uvotimsum and uvotsource with the same aperture used for the transient.

2.3. Spectroscopy

Fifteen optical spectra of SN 2018 fif were obtained using the telescopes and spectrographs listed in Table 3. All the observations were corrected for a Galactic extinction of $E_{B-V} = 0.10$ mag, deduced from Schlafly & Finkbeiner (2011) and using extinction curves of Cardelli et al. (1989).

Following standard spectroscopic reduction, all spectra were scaled so that their synthetic photometry matches contemporaneous P48 r-band values. All spectra are shown in Figure 3 and are available via WISeREP.

3. Analysis

3.1. Epoch of First Light

We fitted the P48 r-band rising flux during the first week with a function of the form

$$f = a(t - t_0)^n, \quad (1)$$

where t_0 is the time of zero flux. This allowed us to estimate the epoch at which the extrapolated r-band light curve turns to zero, which is used throughout this paper as the reference time $t_0({\rm MJD}) = 58{,}351.1537^{+0.0356}_{-0.0903}$ (2018 August 21 at 03:41:19.680 UTC, 0.2 days before the first r-band detection).

3.2. Blackbody Temperature and Radius

Taking advantage of the multiple-band photometric coverage, we derived the temperature and radius of the blackbody that best fit the photometric data at each epoch after interpolating the various data sets to obtain data coverage at coinciding epochs, and deriving the errors at the interpolated points with Markov Chain Monte Carlo simulations. This was performed using the `PhotoFit`[26] tool, which is released in Appendix A. The extinction E_{B-V} was implemented using the extinction curves of Cardelli et al. (1989) with $R_V = 3.08$. The interpolated spectral energy distributions (SEDs) are shown in Figure 4. The derived best-fit temperatures $T_{\rm BB}$ and radii $r_{\rm BB}$ are shown and compared to those derived for SN 2013fs in Figure 5.

3.3. Bolometric Light Curve

Based on the measurement of $r_{\rm BB}$ and $T_{\rm BB}$, we were able to derive the luminosity $L_{\rm BB} = 4\pi r_{\rm BB}^2 \sigma T_{\rm BB}^4$ of the blackbody fits, shown in Figure 6. It is interesting to note that the bolometric peak occurs early on during the UV-dominated hot shock-cooling phase, well before the apparent peak in visible light.

3.4. Spectroscopy

Figure 3 shows the spectroscopic evolution of SN 2018fif over 119 days from its estimated explosion time. The sequence is quite typical for Type II SNe (Gal-Yam 2017), initially showing blue, almost featureless spectra, with low-contrast Balmer lines emerging and becoming pronounced after about a week. The spectrum at phase 15.00 days is typical of the early photospheric phase, with a relatively blue continuum and strong Balmer lines, with Hα showing a strong emission component, Hβ having a symmetric P-Cygni profile, and Hγ appearing only in absorption. The spectra continue to develop as the light curve slowly declines over several months, with the continuum emission growing redder and lines becoming stronger. The latest spectra approach the nebular phase and are dominated by a strong emission component of the Hα line, emerging emission lines of Ca II (at λ7300 as well as the near-IR triplet), weaker O I (λ7774 and a hint of λ6300), and Na D.

[23] https://wiserep.weizmann.ac.il
[24] https://heasarc.gsfc.nasa.gov/cgi-bin/W3Browse/swift.pl
[25] https://heasarc.nasa.gov/lheasoft/
[26] https://github.com/maayane/PhotoFit

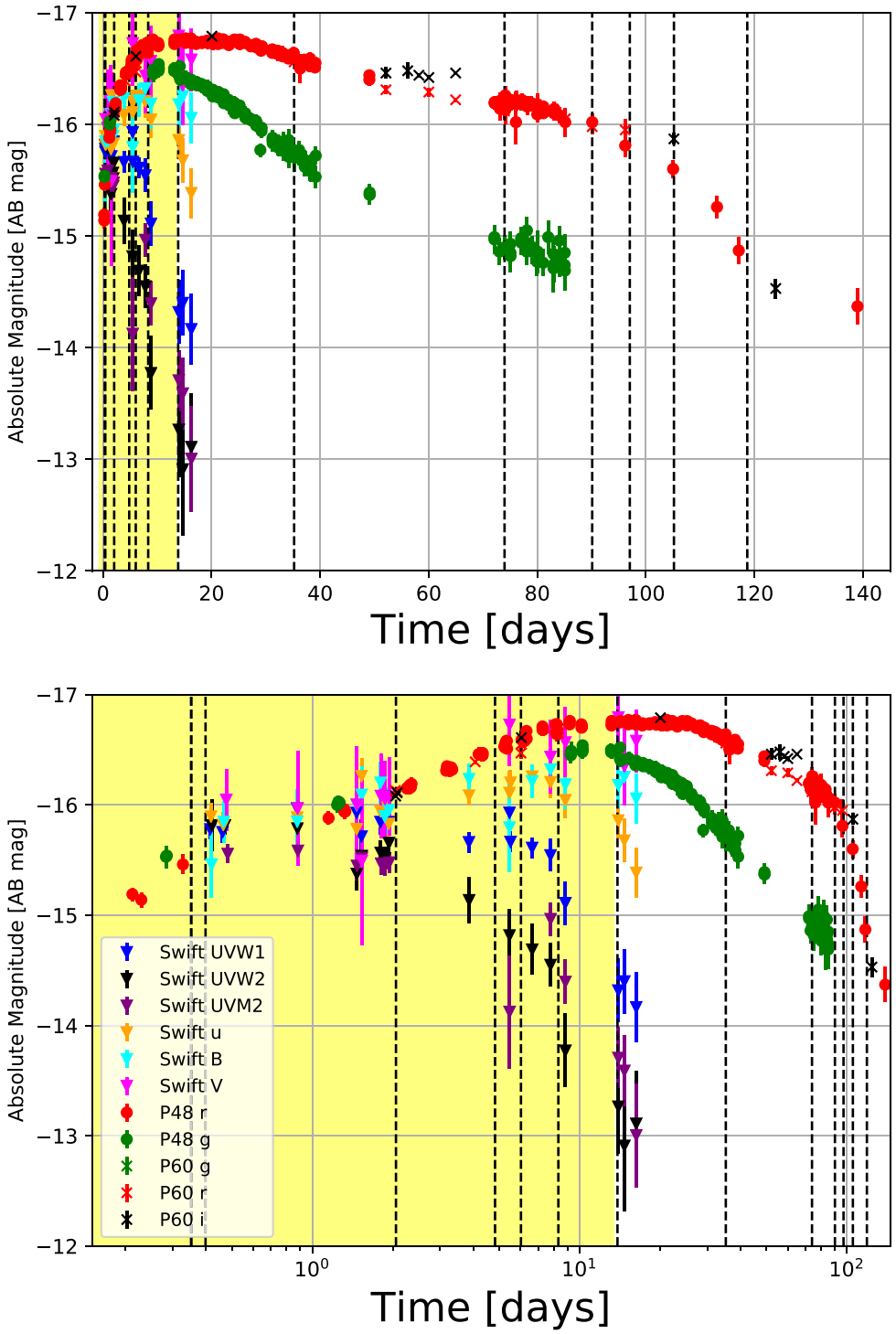

Figure 2. The light curve of SN 2018 fif in linear (top panel) and logarithmic space (lower panel). Time is shown relative to the estimated epoch at which the extrapolated light curve (Equation (1)) turns to zero: t_0 = 2,458,351.6537 (Julian date, JD), as derived in Section 3.1. Black dashed lines indicate dates at which spectroscopic data exist. The yellow background indicates the validity domain of the M20 best fit model: [0.062, 14.107] days relative to the model explosion epoch $t_{\rm ref}$, i.e., [−0.641, 13.403] days relative to t_0.

Focusing on the earliest phase, in Figure 7, we show a comparison of the early spectra of SN 2018fif (P200/DBSP and Gemini-N/GMOS at +8.4 and +8.7 hr from the estimated explosion time, respectively) with the +21 hr NOT/ALFOSC spectrum of SN 2013fs (Yaron et al. 2017), which is most similar to our data. We note that earlier spectra of SN 2013fs at a similar phase to those of SN 2018fif (6–10 hr after explosion) are dominated by very strong emission lines of O IV and He II that are not seen in this case.

In the spectrum of SN 2013fs, the hydrogen Balmer lines show a broadened base and characteristic electron-scattering wings that are a measure of the electron density in the CSM. The spectra of

Table 2
Photometric Observations of SN 2018fif

Epoch (JD)	Mag (mag AB)	Flux (10^{-17} erg s^{-1} cm^{-2} Å^{-1})	Instrument
2,458,351.866	19.11 ± 0.06	5.756 ± 0.318	P48/R
2,458,351.937	18.78 ± 0.10	15.10 ± 1.391	P48/G
2,458,353.697	18.18 ± 0.02	15.263 ± 0.281	P60/r'
2,458,353.699	18.17 ± 0.03	26.563 ± 0.734	P60/g'
2,458,353.7021	18.23 ± 0.02	9.907 ± 0.183	P60/i'
2,458,352.067	18.55 ± 0.10	62.282 ± 5.992	Swift/UVW1
2,458,352.074	18.48 ± 0.23	104.091 ± 22.299	Swift/UVW2
2,458,352.132	18.71 ± 0.09	70.281 ± 6.024	Swift/UVM2
2,458,352.071	18.36 ± 0.13	40.883 ± 4.793	Swift/u

(This table is available in its entirety in machine-readable form.)

SN 2018fif do not show such electron-scattering signatures, even at a much earlier time, and the narrow emission lines seem to arise only from host galaxy emission, with similar profiles to other host lines (such as N II and S II, evident right next to the Hα line). A signature of some CSM interaction may appear in the blue part of the spectrum, in a ledge-shaped emission bump near λ4600. This shape is similar to that seen in the spectrum of SN 2013fs, though the sharp emission spikes (in particular of He II λ4686) are less well defined. The inset in Figure 7 shows a zoom-in of the elevated region around the He II λ4686 emission line for the spectra of both SN 2018fif +8.7 hr and SN 2013fs +21 hr. Possible emission lines that may contribute to this elevated emission region include N V λ4604, N II λ4631, λ4643, and C IV λ4658. Although these identifications are not certain (since they are based on single lines that are only marginally above the noise level), it appears likely that a blend of high-ionization lines is responsible for the elevated emission above the blue continuum.

The difference between the spectra of SN 2013fs and SN 2018fif at ∼8 hr, and in particular the fact that SN 2013fs showed much stronger lines of higher ionization species at similar epochs, suggest that the progenitor of SN 2018fif was surrounded by less nearby CSM than the progenitor of SN 2013fs. The lack of strong high-ionization lines in the spectra of SN 2018fif, as well as the sharp profiles of the Balmer lines that show no evidence of electron-scattering wings, suggests that the CSM that did surround the progenitor of SN 2018fif was likely less dense than in the case of SN 2013fs.

4. Shock Cooling and Progenitor Model

4.1. The Model

In order to model the multiple-band emission from SN 2018fif, we used the model of Sapir & Waxman (2017), an extension of the model derived in Rabinak & Waxman (2011). In the following, the abbreviations "SW17" and "RW11" are used to refer to the models. We summarize below the main conclusions of these two models. Both hold for temperatures >0.7 eV, the limit above which hydrogen is fully ionized, where recombination effects can be neglected and the approximation of constant opacity holds. We emphasize that the results presented here depend on the assumptions adopted by the SW17 analytical model we use, and that other approaches—in particular using hydrodynamical codes—exist and could be used for modeling our observations.

4.1.1. The Model of Rabinak & Waxman (2011)

Rabinak & Waxman (2011) explored the domain of times when the emission originates from a thin shell of mass, i.e., the radius of the photosphere is close to the radius of the stellar surface. The postbreakout time evolution of the photospheric temperature and bolometric luminosity is given below (see also Equation (4) of Sapir & Waxman 2017), where the prefactors correspond to different power-law indices for the density profiles close to the stellar surface (i.e., at radii r such that $\delta \equiv (R-r)/R \ll 1$) $\rho \propto \delta^n$ with $n = 3/2$ [3] for convective [radiative] polytropic envelopes (see Equation (1) in Sapir & Waxman 2017):

$$T_{\rm ph,RW} = 1.61[1.69]\left(\frac{v_{s*,8.5}^2 t_{\rm d}^2}{f_\rho M_0 \kappa_{0.34}}\right)^{\epsilon_1} \frac{R_{13}^{1/4}}{\kappa_{0.34}^{1/4}} t_{\rm d}^{-1/2}\ {\rm eV}, \quad (2)$$

$$L_{\rm RW} = 2.0[2.1]\times 10^{42}\left(\frac{v_{s*,8.5}t_{\rm d}^2}{f_\rho M_0 \kappa_{0.34}}\right)^{-\epsilon_2} \frac{v_{s*,8.5}^2 R_{13}}{\kappa_{0.34}}\ {\rm erg\ s^{-1}}, \quad (3)$$

where $\kappa = 0.34\kappa_{0.34}$ cm^2 g^{-1}, $v_{s*} = 10^{8.5}\, v_{s*,8.5}$, $M = M_0 M_\odot$, $R = 10^{13} R_{13}$ cm, $\epsilon_1 = 0.027$ [0.0.016], and $\epsilon_2 = 0.086$ [0.175]. M is the mass of the ejecta, f_ρ is a numerical factor of order unity describing the inner structure of the envelope, $t_{\rm d}$ is the time from explosion in days, and v_{s*} is a measure of the shock velocity $v_{\rm sh}$; in regions close to the stellar surface, $v_{\rm sh}$ is linked to v_{s*} through (Gandel'Man & Frank-Kamenetskii 1956; Sakurai 1960)

$$v_{\rm sh} = v_{s*}\delta^{-\beta n}, \quad (4)$$

where $\beta = 0.191$ [0.186], $n = 3/2$ [3], and where v_{s*} only depends on E, M (the ejecta energy and mass), and f_ρ (Matzner & McKee 1999):

$$v_{s*} \approx 1.05 f_\rho^{-\beta}\sqrt{E/M}, \quad (5)$$

The RW11 model holds over a limited temporal range. The upper limit on this range,

$$t < 3 f_\rho^{-0.1}\frac{\sqrt{\kappa_{0.34}M_0}}{v_{s*,8.5}}\ {\rm days}, \quad (6)$$

follows from the requirement that the emitting shell carry a small fraction of the ejecta mass. The lower limit,

$$t > 0.2\frac{R_{13}}{v_{s*\ 8.5}}\max\left[0.5, \frac{R_{13}^{0.4}}{(f_\rho \kappa_{0.34} M_0)^{0.2} v_{s*\ 8.5}^{0.7}}\right], \quad (7)$$

comes from two different requirements: (1) the photosphere must have penetrated beyond the thickness at which the initial breakout happens (see Equation (16) of RW11) and (2) expansion must be significant enough so that the ejecta are no longer planar and have become spherical (Waxman & Katz 2017); this last requirement was added to the model of Sapir & Waxman (2017).

4.1.2. The Model of Sapir & Waxman (2017)

Sapir & Waxman (2017) extended the RW11 description to later times, when the photosphere has penetrated more deeply

Table 3
Spectroscopic Observations of SN 2018fif

Date (2018 UT)	Phase (days)	Facility [Ref.]	Exp. T (s)	Grism/Grating	Slit (arcsec)	R	Range (Å)
08-21-12:08:32	+0.35	P200/DBSP [1]	900	600/4000 + 316/7500	1.5	···	3310–9190
08-21-12:08:01	+0.35	P60/SEDM [3, 4]	2430	IFU		∼100	3700–9300
08-21-12:25:04	+0.40	Gemini-N/GMOS [2]	900 × 4	B600	1.0	1688	3630–6870
08-23-04:59:25	+2.05	P60/SEDM [3, 4]	1440	IFU		∼100	3700–9300
08-25-23:25:40	+4.82	LT/SPRAT [5]	300		1.8	350	4020–7960
08-27-04:22:22	+6.03	P60/SEDM [3, 4]	1440	IFU		∼100	3780–9220
08-29-11:22:34	+8.32	P60/SEDM [3, 4]	1440	IFU		∼100	3780–9200
09-05-03:46:42	+15.00	NOT/ALFOSC	1800	Grism 4	1.0	360	3410–9670
09-25-08:33:17	+35.20	P60/SEDM [3, 4]	1440	IFU		∼100	3780–9220
11-03-02:50:19	+73.96	P60/SEDM [3, 4]	1600	IFU		∼100	3780–9220
11-14-07:53:52	+85.17	P60/SEDM [3, 4]	1200	IFU		∼100	3780–9220
11-19-06:25:58	+90.11	P60/SEDM [3, 4]	1200	IFU		∼100	3780–9220
11-26-04:39:18	+97.04	P60/SEDM [3, 4]	1200	IFU		∼100	3780–9220
12-04-07:48:03	+105.17	P60/SEDM [3, 4]	1200	IFU		∼100	3780–9220
12-17-20:01:45	+118.68	WHT/ACAM [6]	1500 × 2	V400	1.0	450	4080–9480

Note. [1] Oke & Gunn (1982), [2] Oke et al. (1994), [3] Blagorodnova et al. (2018), [4] Rigault et al. (2019), [5] Steele et al. (2004), [6] Benn et al. (2008).

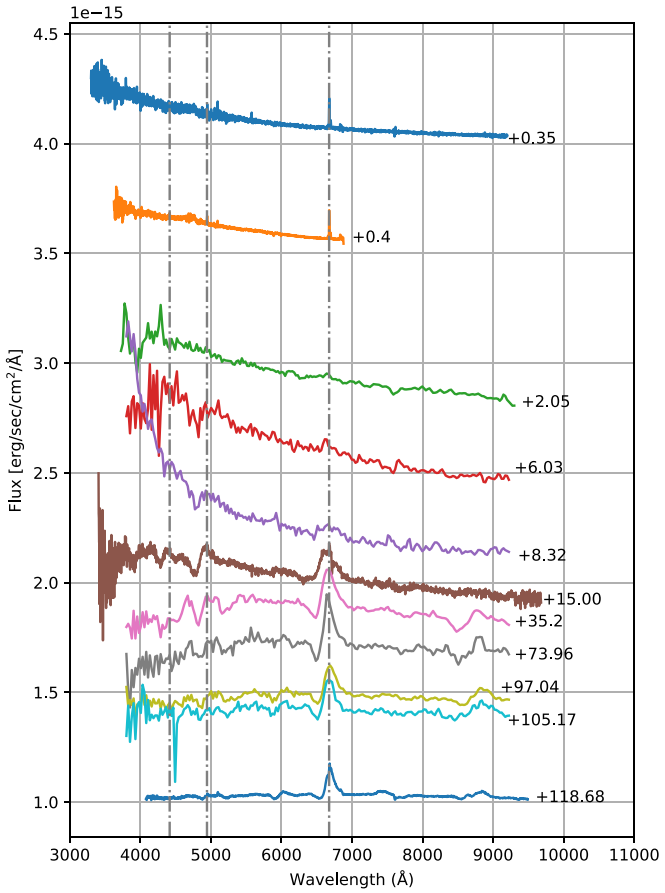

Figure 3. The observed spectra of SN 2018fif. An offset was applied for easier visualization. Dashed lines indicate the redshifted emission lines for the Balmer series up to Hγ. The phase is shown relative to the estimated epoch at which the extrapolated r-band light curve (based on Equation (1)) turns to zero: t_0 = 2,458,351.6537 (2018 August 21), as derived in Section 3.1.

into the envelope but is still close enough to the surface so that the emission is still weakly dependent on the inner structure of the envelope. As radiation originates from inner regions, the self-similar description of the shock wave (Gandel'Man & Frank-Kamenetskii 1956; Sakurai 1960), one of the key ingredients of the RW11 model, does not hold anymore. This results in a suppression of the bolometric luminosity that can be approximated by (Equation (14) of Sapir & Waxman 2017)

$$L/L_{\rm RW} = A\exp\left[-(at/t_{\rm tr})^{\alpha}\right], \tag{8}$$

where $A = 0.94$ [0.79], $a = 1.67$ [4.57], and $\alpha = 0.8$ [0.73] for convective [radiative] envelopes. The thin-shell requirement (Equation (6)) is relaxed, and the new upper limit of the valid time range is dictated by the requirement of constant opacity:

$$t < \min(t_{\rm tr}/a,\, t_{T<0.7}), \tag{9}$$

where $t_{\rm tr}$ is the time beyond which the envelope becomes transparent, and $t_{T<0.7}$ is the time when T drops below 0.7 eV and recombination leads to a decrease in the opacity.

The observed flux, for an SN at luminosity distance D and redshift z, is given by

$$f_\lambda(\lambda, t) = \frac{L(t)}{4\pi D^2 \sigma T_{{\rm col},z}^4} B_\lambda(\lambda, T_{{\rm col},z}) \tag{10}$$

where $T_{{\rm col},z} = T_{\rm col}/(z+1)$ is the temperature of a blackbody with intrinsic temperature $T_{\rm col}$, observed at redshift z, $T_{\rm col}/T_{\rm ph,RW} = 1.1$ [1.0] $\pm$ 0.05 for convective [radiative] envelopes, L is the bolometric luminosity given in Equation (8), and B_λ is the Planck function

$$B_\lambda = \frac{2\pi hc^2}{\lambda^5}\frac{1}{e^{\frac{hc}{\lambda k_B T}} - 1}. \tag{11}$$

4.1.3. The Morag, Sapir & Waxman Extension to Early Times

J. Morag et al. (2020, in preparation) further extend the prescription of Sapir & Waxman (2017) to account for the transition from a planar shock breakout to a spherical self-similar motion of the ejecta. The new prescription is still described by Equation (10), but with a modified luminosity and

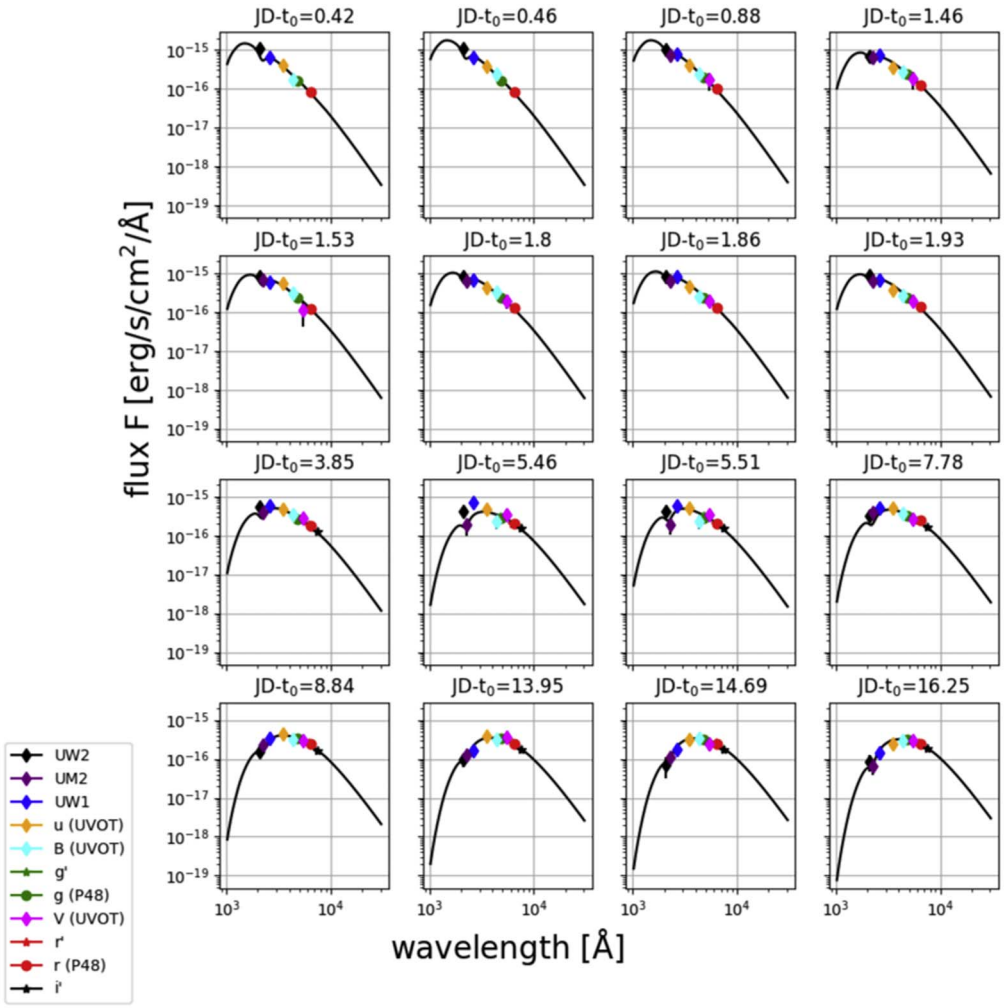

Figure 4. Blackbody fits to Swift/UVOT and optical photometry for SN 2018fif. Using the `PhotoFit` tool (released in Appendix A), photometric points were interpolated to a common epoch (UVOT epochs), and the errors at the interpolated points were computed with Markov Chain Monte Carlo simulations.

temperature. The new composite luminosity L_C is given by

$$L_C = L_{\rm planar} + L_{\rm SW} \tag{12}$$

where $L_{\rm SW}$ is given in Equation (8), and

$$L_{\rm planar} = 2.974 \times 10^{42} \frac{R_{13}^{0.462} v_{\star,85}^{0.602}}{(f_\rho M_0 \kappa_{34})^{0.0643}} \frac{R_{13}^2}{\kappa_{34}} t_h^{-4/3} \ {\rm erg\ s^{-1}}. \tag{13}$$

$L_{\rm planar}$ is the planar-stage postbreakout luminosity as given by Equation (23) in Sapir et al. (2011), cast in terms of SW17 variables. Note that t_h in hours has replaced t_d in days. Likewise, the color temperature is given by

$$T_C = f_T \min\left[T_{\rm planar}, T_{\rm ph,RW}\right] \tag{14}$$

where $T_{\rm ph,RW}$ is the photosphere temperature given in Equation (2), not including the SW17 color factor of 1.1. Meanwhile,

$$T_{\rm planar} = 6.937 \frac{R_{13}^{0.1155} v_{\star,85}^{0.1506}}{f_\rho^{0.01609} M_0^{0.01609} \kappa_{34}^{0.2661}} t_h^{-1/3} \ {\rm eV} \tag{15}$$

is the postbreakout temperature during the planar stage, as given by Sapir et al. (2013) (Section 3.2). A color factor of $f_T = 1.1$ is still an appropriate choice, as calibrated against a set of gray diffusion simulations for a wide range of progenitors and explosion energies.

The new emission accounts for light travel-time effects (Katz et al. 2012) and has the important advantage that it agrees with gray diffusion simulations as early as $t = 3R_\star/c = 17R_{13}$ min after breakout. Thus, we are able to ignore the early SW17 validity times (Equation (7)) and include all the early data points immediately following breakout in our fit.

4.2. The SOPRANOS Algorithm

The main difficulty in implementing the SW17 model is that the temporal validity domain of the model depends on the parameters of the model themselves. In other words, different combinations of the model's parameters correspond to different data to fit (Rubin & Gal-Yam 2017). One way to cope with this difficulty is to fit the data for a chosen range of times, and to retrospectively assess whether the solution is valid in this temporal window. This approach, which was taken, e.g., by Valenti et al. (2014), Bose et al. (2015), Rubin et al. (2016), and Hosseinzadeh et al. (2019), is not fully satisfactory for several reasons: (1) it may limit the area explored in the parameter space, since this area is predefined by the choice of

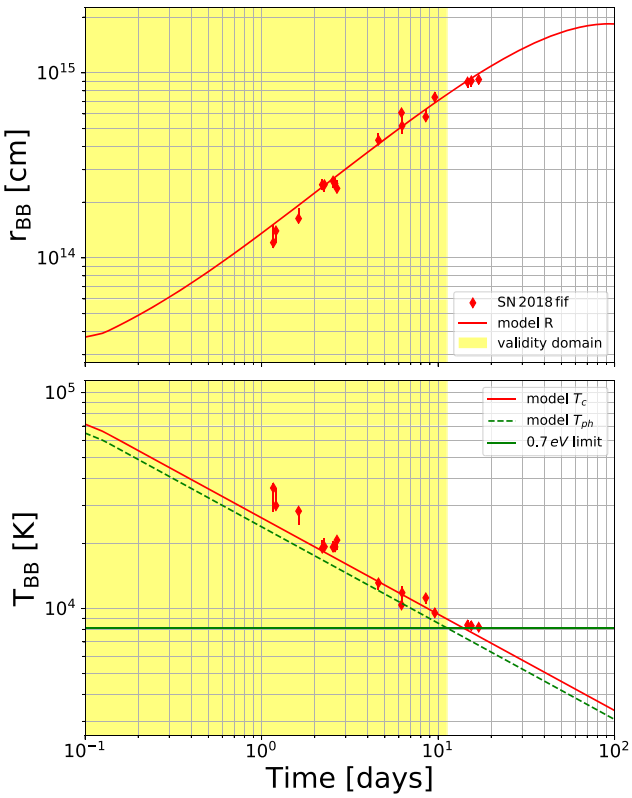

Figure 5. The evolution in time of the radius (top) and the temperature (bottom) of a blackbody with the same radiation as SN 2018fif (red). The points were obtained using the `PhotoFit` code (released in Appendix A). The reference time is the best-fit t_{exp}. The yellow background indicates the temporal validity domain of the M20 best fit model: [0.062, 14.107] days relative to t_{exp}. The red continuous line indicates the radius R and color temperature T_{col} predicted by M20 for the best fit model. The green dashed line indicates $T_{ph,RW}$ (linked to T_{col} through $T_{col}/T_{ph,RW} = 1.1\ [1.0] \pm 0.05$, see Section 4.1.2) and the continuous green line shows the temperature 0.7 eV. The time at which $T_{ph,RW}$ drops below 0.7 eV defines the upper limit of the temporal validity window.

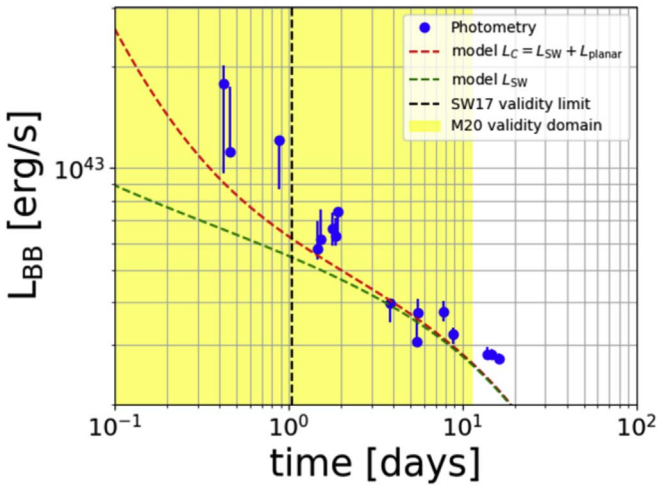

Figure 6. The evolution in time of the bolometric luminosity of a blackbody with the same radiation as SN 2018fif. The green and red dashed lines show the SW17 and M20 predictions, respectively. The yellow background indicates the validity domain of the M20 best fit model: [0.062, 14.107] days relative to t_{exp}, while the black dashed line shows the lower limit of the temporal validity window of the SW17 model for the same set of the progenitor's parameters.

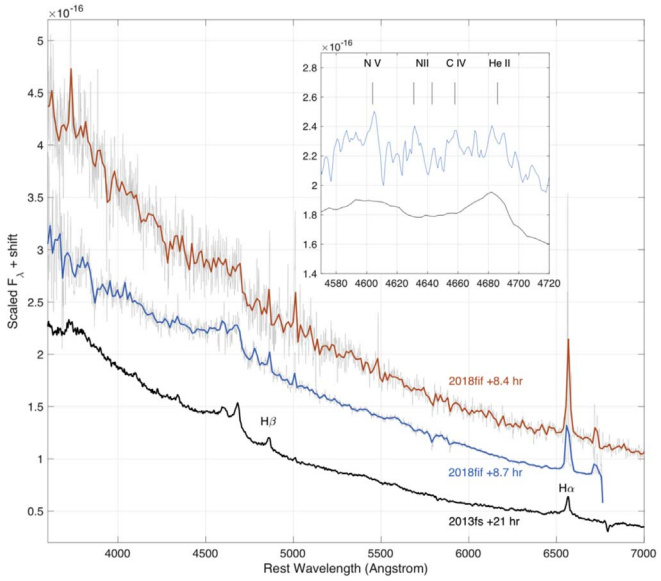

Figure 7. Comparison of early spectra of SN 2018fif (at 8.4 and 8.7 hr) and SN 2013fs (at 21 hr; from Yaron et al. 2017). SN 2018fif shows sharp, narrow Balmer lines lacking a broad electron-scattering base. A broad ledge around 4600 Å indicates a likely blend of weak high-ionization lines, suggesting that some CSM emission does exist in this event, though less than in SN 2013fs; see text.

the data temporal window and (2) it makes it impossible to make a fair comparison between models, because the goodness of a model should be judged on nothing more nor less than its specific validity range: a good model fits the data in its *entire* validity range and *only* in its validity range. It is clear that the best-fit model (and hence deduced progenitor parameters) may depend on the arbitrary choice of predefined data modeled, which is not a good result.

Here, we adopt a self-consistent approach and build an algorithm to find models that fit well the data included in their entire range of validity. In this sense, our approach is similar to the one adopted by Rubin & Gal-Yam (2017). The `SOPRANOS` algorithm (shock-cooling modeling with the Sapir & Waxman model by Ganot & Soumagnac) is available in two versions: `SOPRANOS-grid`, written in `matlab`, and `SOPRANOS-nested`, written in `python` (N. Ganot et al. 2020, in preparation). The steps of `SOPRANOS-grid` are as follows:

1. we build a six-dimensional grid of parameters $\{R, v_{s*,8.5}, t_{ref}, M, f_\rho, E_{B-V}\}$: a given point in the grid (indexed, e.g., j, for clarity) corresponds to a model $\mathcal{M}_j$;
2. we calculate, for each point in the grid, the temporal validity domain, and deduce from it the set of N_j data points $\{x_i, y_i\}_{i \in [1,N_j]}$ (with uncertainties σ_{y_i} on the y_i values) to be taken into account in the fit of model $\mathcal{M}_j$ to the data;
3. we calculate a probability for each point in the grid, using

$$P_j = \mathrm{PDF}(\chi^2_j, \nu_j), \tag{16}$$

where ν_j is the number of degrees of freedom (this number varies between models, as the validity domain—and hence the number of points included in the data—varies), χ^2_j is the chi-square statistic of the fit, for the

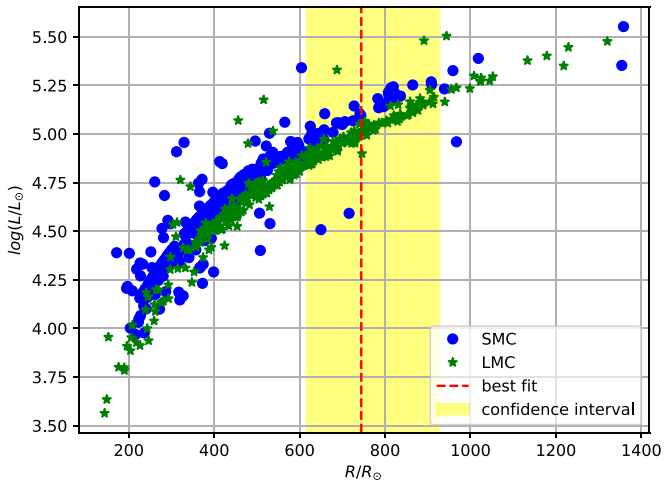

Figure 8. Radii and luminosities of the stars in the Small and Large Magellanic Clouds, derived from the effective temperatures and luminosities published by Davies et al. (2018). The dashed line shows the best-fit solution for SN 2018fif and the yellow background shows the confidence interval.

model $\mathcal{M}_j$,

$$\chi^2_j = \sum_{i=1}^{N_j} \frac{(y_i - \mathcal{M}_j(x_i))^2}{\sigma^2_{y_i}} \quad (17)$$

and PDF is the chi-squared probability distribution function.

The output of this procedure is a grid of probabilities, which we can compare to each other to find the most probable model.

The fluxes $\mathcal{M}_j(x_i)$ are calculated based on Equation (10). The extinction E_{B-V}, a free parameter of the model, is applied to the full spectrum using the extinction curves by Cardelli et al. (1989) with $R_V = 3.08$. Synthetic photometry is then computed using an adaptation of the `pyphot` algorithm routines[27] (M. Fouesneau 2020, in preparation), to convert the monochromatic fluxes f_λ into band fluxes.

The second version of the `SOPRANOS` algorithm, `SOPRANOS-nested`, uses the model probability defined in Equation (16) as the input of the nested sampling algorithm `dynesty` (Skilling 2004, 2006; Higson et al. 2019; Speagle 2020).

In both cases, we apply the following flat priors for the six parameters of our model: $R \in [200, 1500]$, $v_{s*,8.5} \in [0.3, 1.5]$, $M \in [2, 25]$, $f_\rho \in [\sqrt{1/3}, \sqrt{10}]$ (Sapir & Waxman 2017), $t_{\rm ref} \in [2{,}458{,}347.5, t_0]$, $E_{B-V} \in [0.1, 0.35]$. The prior on the radius R was chosen to reflect the bulk of current measurements (Davies et al. 2018; see Figure 8 and Section 5 for a discussion on higher radii). The prior on $f_\rho \in [\sqrt{1/3}, \sqrt{10}]$ corresponds to the range used in the model by Sapir & Waxman (2017). The choice of priors for $t_{\rm ref}$, $v_{s*,8.5}$, and $E_{B-V} \in [0.1, 0.35]$ is the result of an iterative process (coarse to fine grid) aiming at finding the relevant location in the parameter space while limiting the memory use and running time. In all our analysis, we use $\kappa = 0.34\ {\rm cm^2\ g^{-1}}$ and assume a convective envelope for the progenitor. The NOT spectrum taken on 2018 September 5 (JD = 246,366.5, phase +15.00, see Figure 3), showing strong hydrogen lines with P-Cygni profiles, gives an upper limit on the time of recombination, beyond which the SW17 and M20 models are not valid. In practice, recombination is likely to have occurred several days before the emergence of such strong P-Cygni profiles, but in the absence of earlier spectra showing such patterns, this gives a conservative prior on the temporal validity of the models, which we also implement in our algorithm.

Note that our approach is similar to the one by Rubin & Gal-Yam (2017), in the sense that it is self-consistent and takes care of the temporal validity issue. However, the strategy adopted to compare and discriminate between models (Equation (16)) is different. Another difference is the use of the M20 model, which allows us to ignore the SW17 lower limit of the temporal validity window and use all the early data.

4.3. Results

In Figure 9, we show the one- and two-dimensional projections of the probability distribution function distributions obtained by fitting our model to the data with `SOPARANO-nested`. A full tabulation of the best-fit parameters, as well as the 68.2% confidence range for each parameter, is shown in Table 4. For the best-fit values, we report the maximum posterior distribution values computed by `dynesty` : $R = 744.0^{+183.0}_{-128.0}\ R_\odot$, $M_{\rm ej} = 9.3^{+0.4}_{-5.8}\ M_\odot$, $t_{\rm exp} = 2{,}458{,}350.95^{+0.13}_{-0.2}$ JD, $f_\rho = 1.04^{+1.4}_{-0.36}$, $E_{B-V} = 0.199^{+0.036}_{-0.019}$, $v_{s*,8.5} = 0.828^{+0.052}_{-0.118}$, giving $\chi^2/{\rm dof} = 1.67$. In Figure 10, we show a comparison of the observed data and the best-fit model, and in Figure 5 we show a comparison of the blackbody temperature and radius measured from the data and predicted by the best-fit model.

Note that when the probability function is not purely Gaussian (e.g., if it is double-peaked, which is the case here) or is asymmetric, the maximum probability does not necessarily fall close to the median of the marginalized distributions. In particular, it can fall outside of the symmetric interval containing 68% of the probability, which is often reported as the 1σ confidence range, and does not reflect any asymmetry of the distribution. Here, we report instead the tightest intervals containing 68% of the probability and including our best-fit values. We comment on the best-fit results below.

1. In Figure 8, we show red supergiant (RSG) radii and luminosities derived from the temperatures and luminosities measured by Davies et al. (2018) for RSGs in the small and large Magellanic Clouds (SMC and LMC). The best-fit value of the radius we find for the SN 2018fif progenitor star, $R = 744.0^{+183.0}_{-128.0}\ R_\odot$, is well within, but on the large side of, the range of radii measured for RSGs. An important caveat to this comparison is that it holds if the host galaxy of SN 2018fif has a similar metallicity to the Magellanic Clouds (since metallicity affects mass loss and thereby mass, and radius). As can be seen in Figure 1, the SN is located in the outskirts of a spiral galaxy. We do not have sufficient data to estimate the metallicity at the explosion site, but assuming that the galaxy is similar to the Milky Way and has the usual metallicity gradient in spirals, we consider a sub-solar metallicity to be reasonable.
2. The value of $t_{\rm ref}$, the reference time of our model, is earlier than $t_0 = 2{,}458{,}351.6537^{+0.0356}_{-0.0903}$ JD, the estimated epoch at which the extrapolated r-band light curve turns to zero. This is not surprising: t_0 is a measurement of the epoch of first light in the *r band*, and hot young SNe are predicted to emit light in the UV before they significantly emit optical light: there is no reason for t_0 and $t_{\rm ref}$ to be strictly identical.

[27] http://mfouesneau.github.io/docs/pyphot/

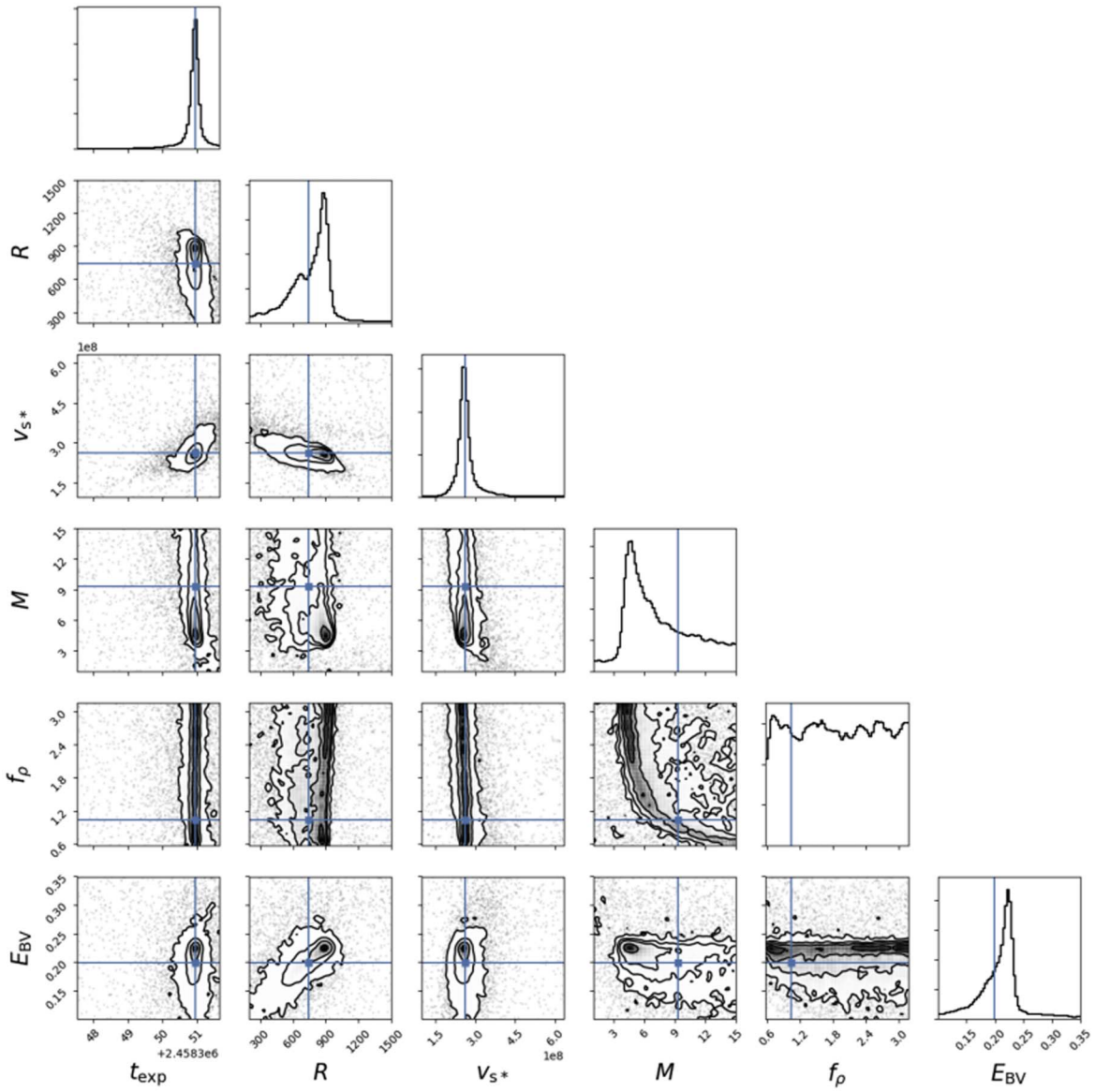

Figure 9. One- and two-dimensional projections of the posterior probability distributions of the parameters R, $v_{s*,8.5}$, M, f_ρ, $t_{\rm ref}$, and E_{B-V}, demonstrating the covariance between parameters. The contours correspond to the 1σ, 2σ, and 3σ symmetric percentiles. The blue line corresponds to the maximum of the posterior distribution, computed by the `dynesty` nested sampling algorithm as part of the `SOPRANOS-nested` package.

Table 4
Results of the Model Fitting

Parameter	Best Fit	Median	68.2% Conf.
R	744.29	804.8	[615.94, 927.61]
$v_{s*,8.5}$	0.828	0.817	[0.71, 0.88]
M	9.3	6.7	[3.5, 9.7]
$t_{\rm exp}$	2,458,350.95	2,458,350.95	[2,458,350.75, 2,458,351.08]
E_{B-V}	0.199	0.215	[0.18, 0.235]
f_ρ	1.04	1.86	[0.68, 2.44]
χ^2/dof	1.69 (263.24/156)	2.29 (357.76/156)	... ...

Note. The table shows the best-fit parameters, the median values of the chains, and the 68.2% confidence range for each parameter, computed using the marginalized posterior distributions.

3. The best-fit value of the extinction $E_{B-V} = 0.199^{+0.036}_{-0.019}$ mag is high: note that it is the sum of the Galactic extinction $E_{B-V} = 0.10$ (deduced from Schlafly & Finkbeiner 2011 and using extinction curves of Cardelli et al. 1989) and all other sources of extinction along the line of sight, including the extinction from the SN host galaxy. The Galactic extinction makes a relatively high contribution to the derived value of E_{B-V}. Moreover, we used the effective wavelength of the Na D lines (in the Gemini spectrum from August 21) in order to estimate the extinction from the host galaxy, following the relation of Poznanski et al. (2012). We found that an estimate of the host extinction is $E_{B-V,\rm host} = 0.10 \pm 0.04$, which, summed with the Galactic extinction, is consistent with the value of E_{B-V} we derived.

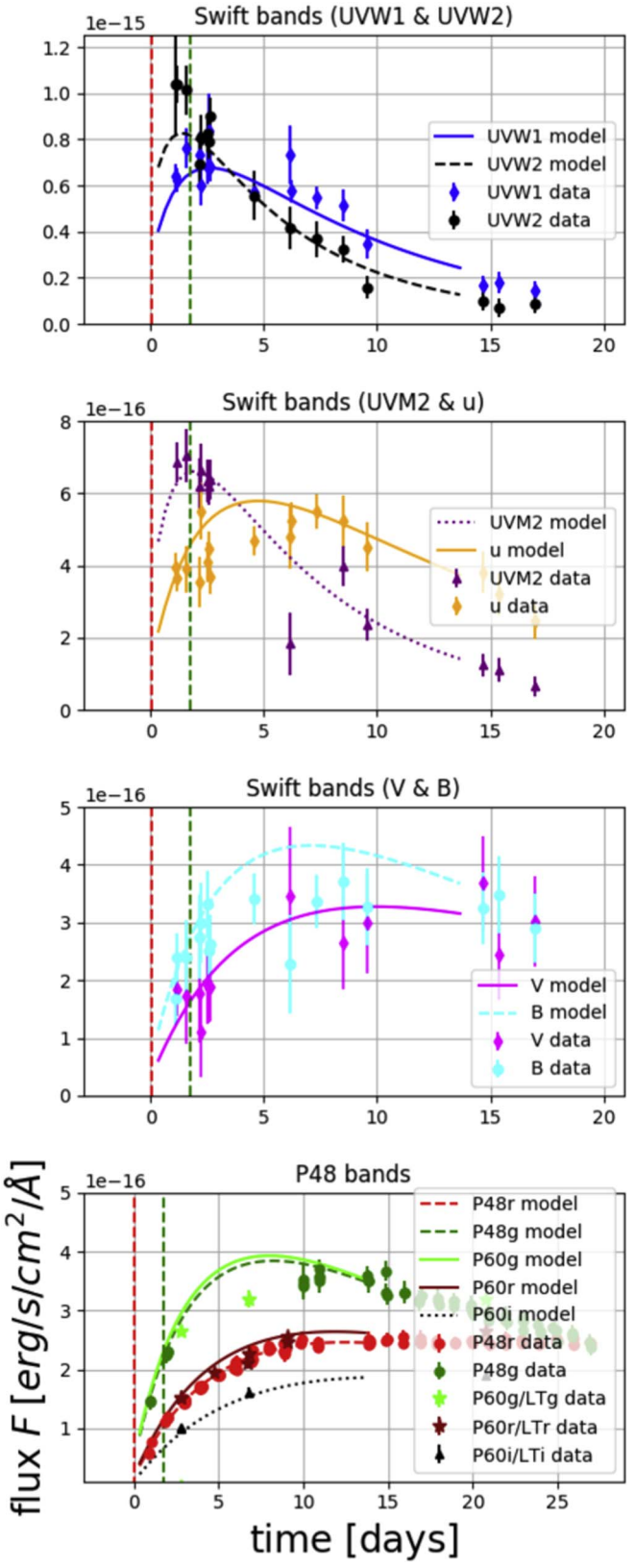

Figure 10. Best -fit model of Morag, Sapir & Waxman (χ^2/dof = 1.69) with the photometric data of SN 2018fif superimposed. The dashed line indicates the lower limit of the temporal validity window for the SW17 (green) and M20 (red) models. The reference date is $t_{\rm ref}$, the explosion epoch predicted by our model.

4. In order to verify whether our best-fit value for $v_{s*,8.5}$ is consistent with the observations, we make an estimate of $v_{\rm sh}$ using our Equation (4) and Equations (11) and (4) from Rabinak & Waxman (2011), which provide an expression of the depth δ as a function of our model parameters and link it to $v_{s*,8.5}$ and $v_{\rm sh}$. Rabinak & Waxman (2011) also link the velocity of the shock to the velocity of the photosphere. We obtain that the predicted value of the velocity of the photosphere is between 10,900 and 12,500 km s^{-1}. Using the P-Cygni profile of the H line in the spectrum of SN 2018fif at $t = +15.00$ days, we estimate the observed velocity $v \approx 10{,}000$ km s^{-1} and find that it is consistent with the model prediction.
5. A connection between M and R exists for hydrostatic stars undergoing secular evolution. This may not be the case for the progenitor just prior to explosion, in particular since it may have lost some mass just shortly prior to exploding. Here, we just report the constraint that the data impose on the parameters of this model, without assuming anything about the status of the progenitor.

Figure 9 shows that the marginalized posterior distribution of radii is double-peaked. In Figure 11, we show the distribution of radii of all the models in the chain and the goodness of fit (χ^2/dof) computed with the first two days of UV data, with a color code for different values of the extinction and recombination time. We find that models with smaller progenitor radii appear to be characterized by lower values of the extinction ($E_{B-V} < E_{B-V,\rm lim} = 0.2$), earlier recombination time ($t_{\rm rec} < t_{\rm rec,lim} = 2{,}458{,}364.65$), and better match to the early UV data. In Appendix B, we show a full tabulation of the results of running `SOPARANO-nested` with narrower priors on the extinction, $E_{B-V} \in [0.15, 0.2]$ and $E_{B-V} \in [0.2, 0.35]$, confirming that the models with lower values of E_{B-V} match the UV data better, and in particular the early UV data.

Although the first spectrum showing clear observational signs that recombination has happened (H lines with strong P-Cygni profiles) was taken at $t = 2{,}458{,}366.65$ (two days after $t_{\rm rec,lim}$), it is reasonable to assume that recombination has happened several days before and that SN 2018fif belongs to the class of objects with smaller radii. If the correlations exhibited in Figure 11 are confirmed with future objects, precisely constraining the time of recombination with denser spectroscopic measurement may help break the extinction/radius degeneracy. As the early UV data seem to distinguish between the two classes of objects, observations of early UV with higher accuracy (e.g., with ULTRASAT) may also enable one to remove the extinction/radius degeneracy, and independently determine both.

4.4. Discussion

Our modeling approach only uses the early part of the light curve. This makes sense, because we only aim at constraining a very limited set of progenitor parameters, mainly its radius R and $E/M_{\rm ej}$, which have been shown (by SW17, using numerical calculations) to determine the early light curve, independently of the stellar density profile or the uncertainties in the explosion models.

However, different modeling approaches exist. In particular, the use of numerical and radiation hydrodynamic codes can

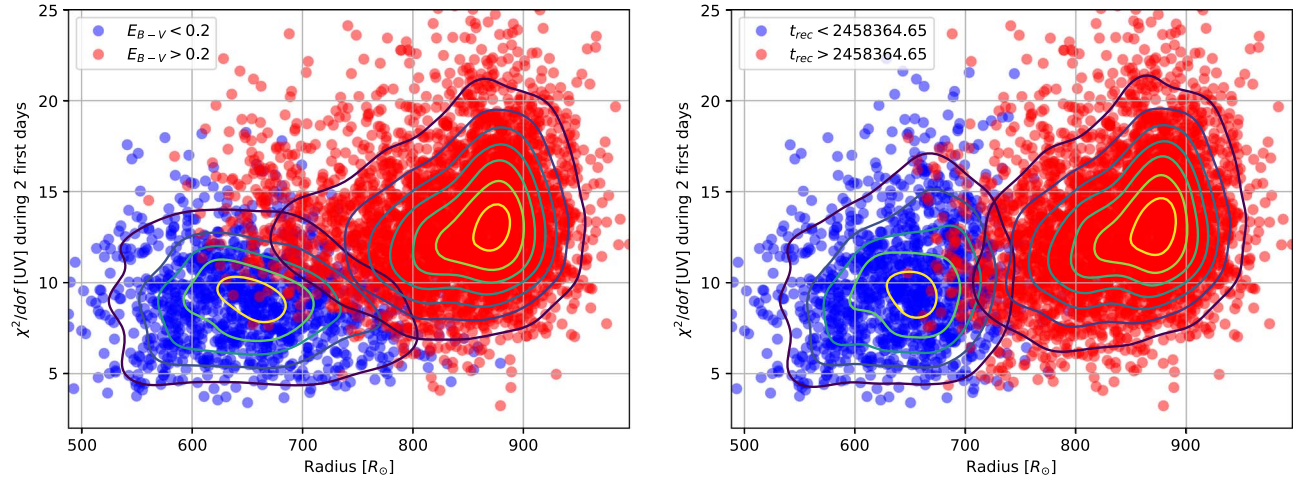

Figure 11. χ^2/dof of all models in the `dynesty` chain, considering only the first two days of UV data, as a function of the model progenitor's radius. The blue and red color coding distinguishes between models with different values of the extinction (left panel) and the time of recombination (right panel). The contours show the density of models. Models (in blue) with $E_{B-V} < 0.2$ and $t_{\rm rec} < 2{,}458{,}364.5$ are characterized by smaller radii and a better match to the early UV data.

allow one to utilize the full light curve, until the late nebular phase, and can be very informative. Below, we give a few examples of recent works adopting or exploring this modeling approach, in order to put our own modeling choices within a broader context.

Several recent works have used radiation hydrodynamic codes to fit models of exploded progenitors to observed light curves. For example, Ricks & Dwarkadas (2019) modeled the full light curve of eight supernovae discovered between 1999 and 2016. They used the stellar evolution code `MESA` (Paxton et al. 2011, 2013, 2015, 2018, 2019) and the radiative transfer code `STELLA` (Blinnikov et al. 1998, 2006; Blinnikov & Sorokina 2004; Baklanov et al. 2005) to evolve stars, explode them, and model their bolometric and individual-band light curves. Assessing the goodness of the fit can be done by fitting the modeled light curves to those of observed SNe for which pre-explosion imaging exists. This strategy was adopted, e.g., by Martinez & Bersten (2019), who modeled the light curves of six SNe that have direct progenitor detection, using a 1D Lagrangian hydrodynamical code. Eldridge et al. (2019) used the STAR code (Eldridge et al. 2017) to model the light curves of 11 SNe with pre-explosion imaging. This approach contrasts with ours in the number of parameters it aims at constraining. Indeed, the fitted parameters include the zero-age main-sequence mass of the progenitor, its rotation velocity, the initial metallicity, parameters governing the mass loss of the star, its core mass, the wind properties that gave rise to the CSM, the explosion energy, the amount of radioactive material synthesized in the explosion as well as its degree of mixing into the outer layers in the ejecta.

Recently, hydrodynamical simulations have suggested that a degeneracy exists, beyond 10–20 days, between the light curves of different families of progenitors, underlying the constraining power of the earliest phase of the light curve. Goldberg et al. (2019) used `MESA` and `STELLA` to show how various families of progenitors produce light curves with similar observables, and explored whether this degeneracy could be broken. Dessart & Hillier (2019) used a 1D Lagrangian hydrodynamical code (Livne 1993; Dessart et al. 2010) to model stars of different mass in order to check whether the SN light curves they produce are different. They found that the different modeled progenitors produced similar light curves between 10 and 100 days and concluded that comparing models and light curves during this phase is not enough to deduce a unique model of the progenitor. This conclusion is in contrast with other works, e.g., by Eldridge et al. (2019)—who claim that it is possible to achieve strong constraints on the progenitors of Type IIp SNe from the light curves alone. Recently, Goldberg & Bildsten (2020) showed that after the first 20 days, families of explosion models with a wide range of $M_{\rm ej}$, R, and E show a good match to the data of five SNe, and that pre-explosion imaging or modeling of the earlier shock-cooling phase is the key to properly constrain the progenitor's properties.

Our approach is therefore complementary to the radiation hydrodynamic modeling approach. It aims at constraining a far smaller set of parameters, at stages of the explosion when radiation hydrodynamic codes often fail to properly model the light curve and before the degeneracy between the light curves of different progenitors becomes an obstacle to their modeling. Combining modeling of the shock-cooling phase with the radiation hydrodynamic modeling approach can break the degeneracy and allow one to use the assets of both approaches for a complete modeling of the progenitor properties.

5. Conclusions

We presented the UV and visible-light observations of SN 2018fif by ZTF and Swift. The analysis of the early spectroscopic observations of SN 2018fif reveals that its progenitor was surrounded by relatively small amounts of CSM compared to a handful of previous cases. This particularity, as well as the high-cadence multiple-band coverage, makes it a good candidate to test shock-cooling models.

We employed the `SOPRANOS` code, an implementation of the model by Sapir & Waxman (2017) and its extension to early times by Morag, Sapir & Waxman (M20; J. Morag et al. 2020, in preparation). The `SOPRANOS` algorithm has the advantage of including a careful account for the limited temporal validity of the shock-cooling model (in this sense, our approach is similar to the one adopted by Rubin & Gal-Yam 2017) as well as allowing usage of the entirety of the early UV data through the M20 extension.

We find that—within the assumptions of the model of Sapir & Waxman (2017)—the progenitor of SN 2018fif was a large red supergiant, with a radius of $R/R_\odot = 744.0^{+183.0}_{-128.0}$ and an

ejected mass of $M/M_{\odot} = 9.3^{+0.4}_{-5.8}$. We find that the distribution of radii is double-peaked, with smaller radii corresponding to lower values of the extinction, earlier recombination times, and a better match to the early UV data. Our model also gives information on the explosion epoch, the progenitor's inner structure, the shock velocity, and the extinction.

Our approach aims at modeling a limited number of key progenitor properties, mainly its radius R and $E/M_{\rm ej}$, using the constraining power of the early stages of the light curve. In this sense it is complementary to recent works that use numerical radiation hydrodynamic codes to model the later stages of the light curve and suffer from the degeneracy between the light curves of various progenitors at later stages (e.g., Goldberg & Bildsten 2020).

As new wide-field transient surveys such as the ZTF (e.g., Bellm et al. 2019; Graham et al. 2019) are deployed, many more SNe will be observed early, and quickly followed up with early spectroscopic observations and multiple-band photometric observations. The ULTRASAT UV satellite mission (Sagiv et al. 2014) will collect early UV light curves of hundreds of core-collapse supernovae. Their high accuracy may enable one to remove the extinction/radius degeneracy and independently determine both. The methodology proposed in this paper offers a framework to analyze these objects, in order to constrain the properties of their massive progenitors and pave the way to a comprehensive understanding of the final evolution and explosive death of massive stars.

We dedicate this paper to the memory of Rona Ramon.

M.T.S. acknowledges support by a grant from IMOS/ISA, the Ilan Ramon fellowship from the Israel Ministry of Science and Technology, and the Benoziyo center for Astrophysics at the Weizmann Institute of Science.

E.O.O. is grateful for the support by grants from the Israel Science Foundation, Minerva, Israeli Ministry of Science, the US–Israel Binational Science Foundation, the Weizmann Institute, and the I-CORE Program of the Planning and Budgeting Committee and the Israel Science Foundation.

A.G.Y.'s research is supported by the EU via ERC grant No. 725161, the ISF GW excellence center, an IMOS space infrastructure grant, and the BSF Transformative program as well as The Benoziyo Endowment Fund for the Advancement of Science, the Deloro Institute for Advanced Research in Space and Optics, The Veronika A. Rabl Physics Discretionary Fund, Paul and Tina Gardner, and the WIS-CIT joint research grant; A.G.Y. is the recipient of the Helen and Martin Kimmel Award for Innovative Investigation.

The data presented here are based—in part—on observations obtained with the Samuel Oschin Telescope 48 inch and the 60 inch Telescope at the Palomar Observatory as part of the Zwicky Transient Facility project. ZTF is supported by the National Science Foundation under grant No. AST-1440341 and a collaboration including Caltech, IPAC, the Weizmann Institute for Science, the Oskar Klein Center at Stockholm University, the University of Maryland, the University of Washington, Deutsches Elektronen-Synchrotron and Humboldt University, Los Alamos National Laboratories, the TANGO Consortium of Taiwan, the University of Wisconsin at Milwaukee, and Lawrence Berkeley National Laboratories. Operations are conducted by COO, IPAC, and UW.

We acknowledge the use of public data from the Swift data archive. This research has made use of data and/or software provided by the High Energy Astrophysics Science Archive Research Center (HEASARC), which is a service of the Astrophysics Science Division at NASA/GSFC.

SED Machine is based upon work supported by the National Science Foundation under grant No. 1106171

The data presented here were obtained—in part—with ALFOSC, which is provided by the Instituto de Astrofisica de Andalucia (IAA) under a joint agreement with the University of Copenhagen and NOTSA.The Liverpool Telescope, located on the island of La Palma in the Spanish Observatorio del Roque de los Muchachos of the Instituto de Astrofisica de Canarias, is operated by Liverpool John Moores University with financial support from the UK Science and Technology Facilities Council. The ACAM spectroscopy was obtained as part of OPT/2018B/011.

Software: `ZTF pipeline` (Masci et al. 2019), `ZOGY` (Zackay et al. 2016), `HEAsoft` (v6.26, HEASARC 2014), `IRAF` (Tody 1986, 1993), `dynesty` (Skilling 2004, 2006; Higson et al. 2019; Speagle 2020), `LRIS pipeline` (Perley 2019), `Astropy` (Astropy Collaboration et al. 2013, 2018), `Matplotlib` (Hunter 2007), `Scipy` (Virtanen et al. 2020).

Appendix A
Release of the `PhotoFit` Code

The `PhotoFit` tool, used to make the figures of this paper, is made available at https://github.com/maayane/PhotoFit. `PhotoFit` is a package for calculating and visualizing the evolution in time of the effective radius, temperature, and luminosity of a supernova—or any target assumed to behave as a blackbody—from multiple-band photometry.

Measurements in different bands are usually taken at different epochs. The first task completed by `PhotoFit` is to interpolate the flux and the errors on common epochs defined by the user.

`PhotoFit` then fits each SED with a blackbody model after (1) correcting for the extinction: PhotoFit does this using Schlafly & Finkbeiner (2011) and using the extinction curves of Cardelli et al. (1989); (2) correcting for the redshift; (3) correcting for the effect of the filter transmission curves: PhotoFit does this using an adaptation of the `pyphot` package routines[28] for synthetic photometry (M. Fouesneau 2020, in preparation).

The fit itself can be done in two different ways (to be chosen by the user and defined in the params.py file):

1. Nested sampling with `dynesty` (Skilling 2004, 2006; Higson et al. 2019; Speagle 2020).
2. A linear fit with a grid of temperatures.

Appendix B
Tabulation of the Solution with Narrow Priors on E_{B-V}

In Table 5, we show a full tabulation of the results of running `SOPRANOS-nested` applying narrow priors on the extinction: $E_{B-V} \in [0.15, 0.20]$ and $E_{B-V} \in [0.20, 0.35]$. The case of lower extinction gives a smaller best-fit radius and a better match to the UV data, specifically the early (first two days) UV data.

[28] http://mfouesneau.github.io/docs/pyphot/

Table 5
Results of the Model Fitting with Narrow Priors on E_{B-V}

Parameter	$E_{B-V} \in [0.15, 0.20]$ Best Fit	Median	68.2% Conf.	$E_{B-V} \in [0.20, 0.35]$ Best Fit	Median	68.2% Conf.
R	533.1	656.29	[486.4, 720.12]	816.29	849.93	[746.16, 979.86]
$v_{s*,8.5}$	0.796	0.831	[0.745, 0.88]	0.793	0.821	[0.71, 0.879]
M	13.9	7.6	[5.8, 14.2]	6.9	6.1	[3.2, 9.4]
t_{exp}	2,458,350.91	2,458,350.93	[2,458,350.82, 2,458,351.07]	2,458,350.94	2,458,350.95	[2,458,350.74, 2,458,351.07]
E_{B-V}	0.151	0.188	[0.15, 0.194]	0.217	0.223	[0.2, 0.23]
f_ρ	1.24	1.81	[0.68, 2.34]	1.88	1.8	[0.58, 2.34]
χ^2/dof	1.77 (264.45/149)	2.28 (339.60/149)	⋯	1.69 (263.99/156)	1.98 (332.95/168)	⋯
χ^2/dof [UV]	1.70 (52.76/31)	1.51 (46.94/31)	⋯	2.40 (74.48/31)	1.78 (60.68/34)	⋯
χ^2/dof [UV, 2 days]	4.64 (9.28/2)	6.89 (13.77/2)	⋯	16.36 (32.72/2)	12.79 (25.57/2)	⋯

Note. The table shows the best-fit parameters, the median values of the dynesty chain, and 68.2% confidence range for each parameter, computed using the marginalized posterior distributions. The two last lines of the table are (respectively) χ^2/dof using only the UV data and only the first two days of UV data.

ORCID iDs

Maayane T. Soumagnac https://orcid.org/0000-0001-6753-1488
Ido Irani https://orcid.org/0000-0002-7996-8780
Avishay Gal-yam https://orcid.org/0000-0002-3653-5598
Eran O. Ofek https://orcid.org/0000-0002-6786-8774
Eli Waxman https://orcid.org/0000-0002-9038-5877
Steve Schulze https://orcid.org/0000-0001-6797-1889
Adam Rubin https://orcid.org/0000-0003-4557-0632
S. Bradley Cenko https://orcid.org/0000-0003-1673-970X
Jesper Sollerman https://orcid.org/0000-0003-1546-6615
Daniel A. Perley https://orcid.org/0000-0001-8472-1996
Christoffer Fremling https://orcid.org/0000-0002-4223-103X
Peter Nugent https://orcid.org/0000-0002-3389-0586
Emir Karamehmetoglu https://orcid.org/0000-0001-6209-838X
Eric C. Bellm https://orcid.org/0000-0001-8018-5348
Rachel J. Bruch https://orcid.org/0000-0001-8208-2473
Virginia Cunningham https://orcid.org/0000-0003-2292-0441
Richard Dekany https://orcid.org/0000-0002-5884-7867
V. Zach Golkhou https://orcid.org/0000-0001-8205-2506
Matthew J. Graham https://orcid.org/0000-0002-3168-0139
Mansi M. Kasliwal https://orcid.org/0000-0002-5619-4938
Shrinivas R. Kulkarni https://orcid.org/0000-0001-5390-8563
Thomas Kupfer https://orcid.org/0000-0002-6540-1484
Russ R. Laher https://orcid.org/0000-0003-2451-5482
Frank J. Masci https://orcid.org/0000-0002-8532-9395
Reed Riddle https://orcid.org/0000-0002-0387-370X
Mickael Rigault https://orcid.org/0000-0002-8121-2560
Ben Rusholme https://orcid.org/0000-0001-7648-4142

References

Arcavi, I., Hosseinzadeh, G., Brown, P. J., et al. 2017, ApJL, 837, L2
Astropy Collaboration, Price-Whelan, A. M., Sipőcz, B. M., et al. 2018, AJ, 156, 123
Astropy Collaboration, Robitaille, T. P., Tollerud, E. J., et al. 2013, A&A, 558, A33
Baklanov, P. V., Blinnikov, S. I., & Pavlyuk, N. N. 2005, AstL, 31, 429
Bellm, E. C., Kulkarni, S. R., Graham, M. J., et al. 2019, PASP, 131, 018002
Bellm, E. C., Kulkarni, S. R. & ZTF Collaboration 2015, AAS Meeting, 225, 328.04
Benn, C., Dee, K., & Agócs, T. 2008, Proc. SPIE, 7014, 70146X
Blagorodnova, N., Neill, J. D., Walters, R., et al. 2018, PASP, 130, 035003
Blinnikov, S., & Sorokina, E. 2004, Ap&SS, 290, 13
Blinnikov, S. I., Eastman, R., Bartunov, O. S., Popolitov, V. A., & Woosley, S. E. 1998, ApJ, 496, 454
Blinnikov, S. I., Röpke, F. K., Sorokina, E. I., et al. 2006, A&A, 453, 229
Bose, S., Valenti, S., Misra, K., et al. 2015, MNRAS, 450, 2373
Cardelli, J. A., Clayton, G. C., & Mathis, J. S. 1989, ApJ, 345, 245
Cenko, S. B., Fox, D. B., Moon, D.-S., et al. 2006, PASP, 118, 1396
Davies, B., Crowther, P. A., & Beasor, E. R. 2018, MNRAS, 478, 3138
Dessart, L., & Hillier, D. J. 2019, A&A, 625, A9
Dessart, L., Livne, E., & Waldman, R. 2010, MNRAS, 408, 827
Eldridge, J. J., Guo, N. Y., Rodrigues, N., Stanway, E. R., & Xiao, L. 2019, PASA, 36, e041
Eldridge, J. J., Stanway, E. R., Xiao, L., et al. 2017, PASA, 34, e058
Falco, E. E., Kurtz, M. J., Geller, M. J., et al. 1999, PASP, 111, 438
Fremling, C. 2018, Transient Name Server Discovery Report 2018-1231
Fremling, C., Sollerman, J., Taddia, F., et al. 2016, A&A, 593, A68
Gall, E. E. E., Polshaw, J., Kotak, R., et al. 2015, A&A, 582, A3
Gal-Yam, A. 2017, in Handbook of Supernovae, ed. A. W. Alsabti & P. Murdin (Cham: Springer), 195
Gal-Yam, A. 2019, AAS Meeting, 233, 131.06
Gal-Yam, A., Arcavi, I., Ofek, E. O., et al. 2014, Natur, 509, 471
Gal-Yam, A., Kasliwal, M. M., Arcavi, I., et al. 2011, ApJ, 736, 159
Gandel'Man, G. M., & Frank-Kamenetskii, D. A. 1956, SPhD, 1, 223
Gehrels, N., Chincarini, G., Giommi, P., et al. 2004, ApJ, 611, 1005
Goldberg, J. A., & Bildsten, L. 2020, ApJL, 895, L45
Goldberg, J. A., Bildsten, L., & Paxton, B. 2019, ApJ, 879, 3
González-Gaitán, S., Tominaga, N., Molina, J., et al. 2015, MNRAS, 451, 2212
Graham, M. J., Kulkarni, S. R., Bellm, E. C., et al. 2019, PASP, 131, 078001
HEASARC 2014, HEAsoft: Unified Release of FTOOLS and XANADU Astrophysics Source Code Library, ascl:1408.004
Higson, E., Handley, W., Hobson, M., & Lasenby, A. 2019, Stat. Comput., 29, 891
Hosseinzadeh, G., McCully, C., Zabludoff, A. I., et al. 2019, ApJL, 871, L9
Hosseinzadeh, G., Valenti, S., McCully, C., et al. 2018, ApJ, 861, 63
Hunter, J. D. 2007, CSE, 9, 90
Kasliwal, M. M., Cannella, C., Bagdasaryan, A., et al. 2019, PASP, 131, 038003
Katz, B., Sapir, N., & Waxman, E. 2012, ApJ, 747, 147
Khazov, D., Yaron, O., Gal-Yam, A., et al. 2016, ApJ, 818, 3
Levesque, E. M. 2017, Astrophysics of Red Supergiants (Bristol: IOP Publishing)
Livne, E. 1993, ApJ, 412, 634
Martinez, L., & Bersten, M. C. 2019, A&A, 629, A124
Masci, F. J., Laher, R. R., Rusholme, B., et al. 2019, PASP, 131, 018003
Matzner, C. D., & McKee, C. F. 1999, ApJ, 510, 379
Morozova, V., Piro, A. L., Renzo, M., & Ott, C. D. 2016, ApJ, 829, 109
Nugent, P. E., Sullivan, M., Cenko, S. B., et al. 2011, Natur, 480, 344
Oke, J. B., Cohen, J. G., Carr, M., et al. 1994, Proc. SPIE, 2198, 178
Oke, J. B., & Gunn, J. E. 1982, PASP, 94, 586
Patterson, M. T., Bellm, E. C., Rusholme, B., et al. 2019, PASP, 131, 018001

Paxton, B., Bildsten, L., Dotter, A., et al. 2011, ApJS, 192, 3
Paxton, B., Cantiello, M., Arras, P., et al. 2013, ApJS, 208, 4
Paxton, B., Marchant, P., Schwab, J., et al. 2015, ApJS, 220, 15
Paxton, B., Schwab, J., Bauer, E. B., et al. 2018, ApJS, 234, 34
Paxton, B., Smolec, R., Schwab, J., et al. 2019, ApJS, 243, 10
Perley, D. A. 2019, PASP, 131, 084503
Poznanski, D., Prochaska, J. X., & Bloom, J. S. 2012, MNRAS, 426, 1465
Rabinak, I., & Waxman, E. 2011, ApJ, 728, 63
Ricks, W., & Dwarkadas, V. V. 2019, ApJ, 880, 59
Rigault, M., Neill, J. D., Blagorodnova, N., et al. 2019, A&A, 627, A115
Rubin, A., & Gal-Yam, A. 2017, ApJ, 848, 8
Rubin, A., Gal-Yam, A., de Cia, A., et al. 2016, ApJ, 820, 33
Sagiv, I., Gal-Yam, A., Ofek, E. O., et al. 2014, AJ, 147, 79
Sakurai, A. 1960, CPAM, 13, 353
Sapir, N., Katz, B., & Waxman, E. 2011, ApJ, 742, 36
Sapir, N., Katz, B., & Waxman, E. 2013, ApJ, 774, 79
Sapir, N., & Waxman, E. 2017, ApJ, 838, 130
Schlafly, E. F., & Finkbeiner, D. P. 2011, ApJ, 737, 103
Shivvers, I., Groh, J. H., Mauerhan, J. C., et al. 2015, ApJ, 806, 213
Skilling, J. 2004, in AIP Conf. Ser. 735, Bayesian Inference and Maximum Entropy Methods in Science and Engineering, ed. R. Fischer, R. Preuss, & U. V. Toussaint (Melville, NY: AIP), 395
Skilling, J. 2006, in AIP Conf. Ser. 872, Bayesian Inference and Maximum Entropy Methods In Science and Engineering, ed. A. Mohammad-Djafari (Melville, NY: AIP), 321
Smartt, S. J. 2015, PASA, 32, e016
Speagle, J. S. 2020, MNRAS, 493, 3132
Steele, I. A., Smith, R. J., Rees, P. C., et al. 2004, Proc. SPIE, 5489, 679
Tartaglia, L., Fraser, M., Sand, D. J., et al. 2017, ApJL, 836, L12
Tody, D. 1986, Proc. SPIE, 627, 733
Tody, D. 1993, in ASP Conf. Ser. 52, IRAF in the Nineties, ed. R. J. Hanisch, R. J. V. Brissenden, & J. Barnes (San Francisco, CA: ASP), 173
Valenti, S., Sand, D., Pastorello, A., et al. 2014, MNRAS, 438, L101
Virtanen, P., Gommers, R., Oliphant, T. E., et al. 2020, NatMe, 17, 261
Waxman, E., & Katz, B. 2017, Handbook of Supernovae (Cham: Springer), 967
Yaron, O., & Gal-Yam, A. 2012, PASP, 124, 668
Yaron, O., Perley, D. A., Gal-Yam, A., et al. 2017, NatPh, 13, 510
Zackay, B., Ofek, E. O., & Gal-Yam, A. 2016, ApJ, 830, 27